3D-printed, biomimetic, conductive MXene-microfiber composite scaffolds enhance the axonal growth-promoting characteristics of electrical stimulation.

Woods I.[1,2], Spurling D.[3], Sunil S.[1], Maughan J.[1,2,4], Guttierez-Gonzales J.[1,2,3], Dervan A.[1,2], Nicolosi V.[3], O'Brien F. J.[1,2*]

Affiliations:

[1]Tissue Engineering Research Group, Department of Anatomy & Regenerative Medicine

Royal College of Surgeons in Ireland (RCSI) 123 St. Stephen's Green, Dublin 2, D02YN77, Ireland

[2]Advanced Materials and Bioengineering Research (AMBER) Centre RCSI 123 St Stephen's Green, Dublin 2, D02YN77, Ireland.

[3]School of Chemistry, Centre for Research on Adaptive Nanostructures and Nanodevices (CRANN) & Advanced Materials Bio-Engineering Research Centre (AMBER), Trinity College Dublin, Dublin 2, Ireland

[4]School of Physics, University of Dublin, Trinity College Dublin (TCD), Ireland

*Corresponding Author: E-mail: fjobrien@rcsi.ie

Abstract:

The application of externally applied electrical stimulation can regulate electrical signalling in neural tissues and has the potential to promote repair of tissue following neurotrauma. Conductive biomaterials can enhance the pro-reparative effects of electrical stimulation by channelling and directing its delivery. $Ti_3C_2T_x$ titanium carbide nanosheets, known as MXenes, are a class of highly conductive (>10^7 S/m) 2D nanomaterials that hold great promise for neural tissue engineering applications. It was hypothesized that functionalizing 3D-printed microfiber scaffolds with MXene nanosheets would produce conductive tissue engineering scaffolds whose tunable electroconductive properties could be adapted to promote axonal growth of seeded neurons in response to extrinsic electrical signals. Melt-electrowriting was used to 3D print polycaprolactone microfiber architectures of varying fiber densities which were coated with a $Ti_3C_2T_x$ MXene ink resulted in highly conductive composite microfiber scaffolds. The electrical conductivity of these microfibrous architectures could be varied in a controlled manner from approximately 0.081 ±0.053 S/m to 18.87 ±2.94 S/m - depending on the microfiber density and layering of MXene ink coatings. The MXene microfiber architectures were filled with a macroporous neurotrophic hyaluronic acid-collagen type-IV/fibronectin biomaterial, designed to mimic the structure and composition of neural tissues and provide an optimal substrate for axonal growth. The application of continuous electrical stimulation (200 mV/mm, 12 Hz) to neurons seeded on the fiber-reinforced biomimetic scaffolds enhanced axonal growth in a manner dependent on the conductive microfiber architecture. These results indicate that optimization of 3D printed conductive microarchitectures can enhance the axonal growth-promoting characteristics of electrical stimulation in a manner dependent on the distribution of conductive material with a tissue engineering scaffold. These biomimetic conductive scaffolds represent a novel approach to the delivery of therapeutic electrical stimulation for neurotrauma repair.

1. Introduction:

Neurotrauma is associated with losses in cognitive, motor and sensory function and can result in paralysis, disability and cognitive difficulties[1]. No effective reparative treatment exists[2]. The complex nature of the pathophysiology of neurotrauma (including inflammation, scarring and poor neuronal regrowth) suggests that a multi-faceted approach may be required to repair central nervous system (CNS) injuries[3]. Biomaterial-based strategies offer platforms which can address aspects of neural injuries[4] and among these strategies, the delivery of electrical stimulation through conductive implants holds some promise. Recently, electrical stimulation (ES) has been shown, *in vitro*, to promote axonal growth[5], enhance neuronal plasticity[6] and support neuronal function[7]. Recent ground-breaking work by Courtine et al. (2023) has shown that, in a chronic spinal cord injury patient, integration of distal ES through a sub-dural implant and brain-computer interface-enabled motor

stimulation promoted permanent improvements in motor function[8], although the mechanism through which this occurred is unknown.

Furthermore, the delivery of ES to neurons via conductive biomaterials enhances the associated benefits[6,9–12]. Patterning of conductive materials into ordered structures allows the manipulation of the electric fields experienced by neurons such as the promotion of orientated axonal growth via stimulation of neurons on aligned conductive fibers[13]. In peripheral nerve repair, powered tubular conductive conduits enhance peripheral nerve regrowth through their lumen, promoting functional recovery following sciatic nerve injuries[6,14]. Furthermore, preclinical studies indicate that injectable hydrogels containing conductive polymers can facilitate limited repair through their conductive characteristics[15,16], but the directed delivery of pro-regenerative ES through a structured conductive scaffold for neurotrauma repair has yet to be achieved.

The most commonly used biomaterials for the therapeutic delivery of ES are metallic electrodes – often used for deep brain stimulation treatments (e.g. for Parkinson's Disease)[17]. These stiff materials exhibit significant limitations including compliance mismatch, poor neurocompatibility and pro-inflammatory properties[18]. In order to overcome these issues a range of softer, more biomimetic conductive biomaterials such as conductive polymers and nanocomposite biomaterials have been developed. However, commonly used conductive polymer-based biomaterials exhibit three key limitations – poor processability[19], low bioactivity and rapid degradation of conductivity in biological environments[20]. In comparison, the key limitation of nanocomposites is the high volume ratios that can be necessary to achieve percolation thresholds to produce conductive bulk materials (leading to high stiffness and low bioactivity)[21]. The incorporation of conductive nanomaterials within natural (e.g. collagen)[22] and synthetic (e.g. PCL)[23] polymers can greatly enhance their neurocompatibility. Ji et al. (2023) combined these approaches to develop a 3D printable PEDOT:PSS-carbon nanotube hydrogel composite which provides a 3D printable, highly conductive, biocompatible interface. 2D nanomaterials such as MXenes, specifically $Ti_3C_2T_x$ nanosheets derived from aluminium-rich MAX phase formulations, are stable, highly conductive and biocompatible – making excellent candidates for conductive nanocomposite design but have yet to be used in tissue engineering applications[11,24].

To facilitate structured incorporation of MXenes into a tissue engineering scaffold, melt electrowriting (MEW) was used to 3D print microfiber architectures. MEW combines the microscale fiber production of electrospinning with the high spatial resolution of 3D printing to print ordered microfibrous structures. By functionalizing these microfibers with MXene nanoflakes to form a novel nanocomposite scaffold, 3D printable scaffolds with tunable conductive properties were produced, in which fiber organization can be used to control electrical properties. These conductive microfiber architectures were then embedded within a biomimetic neurotrophic macroporous scaffold, previously developed as a platform for spinal cord injury repair[25]. This composite scaffold provided a tissue-like matrix for testing the capacity of the conductive microfiber architectures to enhance the delivery of exogenous electrical stimulation to nearby neurons.

The aim of the study was to use 3D printing to optimize the distribution of conductive materials throughout a biphasic scaffold in order to develop a biomaterial implant capable of maximizing the axonal growth-promoting characteristics of electrical stimulation. It was hypothesized that the extrinsic electrical stimulation of the implant through the MXene-functionalized conductive architectures would enhance the growth of axons from neurons within the biomimetic HA phase of the biphasic scaffolds in a manner dependent on microfiber architecture. Examination of the conductive and electrochemical properties of the MXene-PCL frameworks indicated that these properties varied with fiber architecture and MXene density. The MXene microfiber architectures were successfully embedded within macroporous extracellular matrix protein-functionalized hyaluronic acid (HA-ECM), which exhibited a highly porous pore-architecture. Stimulation was carried

out using an IonOptix bioreactor, which was used to deliver a 200 mV/mm pulsed electrical stimulation regime to scaffold samples. Neurons in stimulated conductive scaffolds exhibited significantly longer axons than inert PCL controls. Furthermore, this increase in axonal growth in response to ES was shown to be dependent on MXene-microfiber architecture. These results demonstrate that MXene-PCL composite materials have high conductivity and excellent neurocompatibility. Furthermore, it is shown that conductive MXene-microfiber scaffolds can contribute to improving the pro-reparative characteristics of electrical stimulation and that the spatial organization of conductive scaffolds plays an important role in determining the response of ingrowing neurons to ES.

2. Methods and Materials:

2.1 Materials

All reagents were purchased from Sigma Aldrich (Ireland) unless stated otherwise. Wash steps refer to 3× Dulbecco phosphate buffered saline (DPBS) washes for 5 min at room temperature (RT) unless stated otherwise. All culture conditions were at 37 °C, 5% CO2 unless stated otherwise.

2.2 MXene Synthesis and particle characterization

To a 200 ml HDPE bottle, 9M HCl (40 ml) was added. A PTFE stirrer was placed inside and set to stir at 300 rpm in an ice bath. Once cooled, around 10 minutes, Al-rich Ti_3AlC_2 MAX phase powder (4 g, Carbon-Ukraine ltd.) was added in small additions (c. 400 mg/min) to avoid excessive heating of the solution. The lid was placed loosely on the bottle and the mixture stirred for 18 h to remove excess metals (mostly Al) from the powder. The mixture was then washed several times with deionised water, centrifuging at 5000 rpm using a Thermo Scientific Heraeus Multifuge X1 for 5 minutes each time, until the pH of the supernatant was > 6. The washed MAX phase sediments were then dried via vacuum filtration overnight. The resulting MAX phase powder was then weighed, typically having lost around 25% of its original mass.

To a 200 ml HDPE bottle in a mineral oil bath, 9M HCl (60 ml), followed by LiF powder (4,8g, Sigma) was added, and left to stir using a PTFE stirrer bar for 5 min. The washed MAX phase powder (3g) was then added slowly over 5 min. The solution was then left stirring at 400 rpm, 35°C for 24 hours to obtain the etched, multilayer $Ti_3C_2T_x$ MXene.

To wash, the contents of the vessel were transferred evenly into 2 50 ml centrifuge tubes and diluted to a total of 40 ml each with deionised water. The dispersions were then washed around 10 times via centrifugation at 5000 rpm until the pH of the supernatant was approximately neutral. The tubes were again filled to 40 ml with deionised water and vortex mixed for 1 hour at 1800 rpm to delaminate the MXene. The MXene dispersion was then centrifuged at 1500 rpm for 30 minutes to sediment any multi-layer MXene or unreacted MAX phase that remained. The supernatant containing delaminated MXene flakes was then collected. This supernatant was then centrifuged at 5000 rpm for 1 hour to sediment the few-layer flakes, the sediments were then redispersed in a total of 25 ml deionised water to obtain a concentrated MXene ink.

2.3 Electron Microscopy

SEM analysis of the pore structure of freeze-dried scaffolds was carried out similarly to previously published analyses[25]. Scaffolds were bisected in transverse and longitudinal orientations using microtome blades and prepared for imaging through gold sputter coating. Samples were inserted into the chamber of a Zeiss Ultra Plus field-emission SEM electron microscope (Zeiss, Oberkochen, Germany) and imaged using accompanying SmartSEM software. EDX of the $Ti_3C_2T_x$ was performed at an acceleration voltage of 10 keV with a 20mm² Oxford Inca EDX detector.

2.4 Surface Analysis

2.4.1 Hydrophilicity

The contact angle of each group was determined by a goniometer (optic contact angle measuring and contour analysis system model OCA 25). A water droplet of 100µl is placed upon each film and the contact angle measured.

2.4.2 Atomic Force Microscopy

To assess the surface topography of the MXene-PCL composites, AFM was carried out on a scanning probe microscope (NanoSurf) in tapping mode under ambient conditions using aluminum-coated silicon cantilevers (TAP-190i). Average image sizes were 50 × 50 µm at scan rates of 0.5 Hz with 512 lines per image. Images were analyzed using CoreAFM software (NanoSurf).

2.5 Melt Electrowriting

A RegenHu R200 3D printer with a melt electrowriting (MEW) module was used to produce the microfiber scaffolds. Scaffold architectures were designed on Shaper CAD Software (RegenHu). The fiber design was a rectilinear pattern with varied fiber spacings of 500, 750 and 1000 µm. The orientation of the layers was swapped perpendicularly after each layer to produce a "box-like" architecture. A 50 kDA polycaprolactone polymer was used for microfiber manufacture. The following Mew parameters were used: 5 mm tip-to-collector distance, 10 mm/s translation speed, approximately 5 kV voltage, 50 kDA PCL, heated to 80 °C, 24 G spinneret and a 50 kPA extrusion pressure. The taylor cone was allowed approximately 10 minutes to stabilize prior to each print. The patterns were printed to a 75-layer height with 10 µm diameter fibers to produce 750 µm-tall scaffolds. Fiber diameter (n=6) was measured using scanning electron microscopy.

2.6 Electrical Properties

2.6.1 Conductivity Analysis

Film conductivity measurements were performed using an Ossila four-point probe, with a probe spacing of 1.27 mm. Bulk electrical conductivity was determined using the two-point probe method with a probe head (SP4-40180TRJ, Lucas Signatone) connected to a source meter instrument (Model 2450, Keithley). 20 mm x 20 mm microfiber architectures were placed between two carbon electrodes and reading made in a dry state at RT. Current readings were obtained by sourcing voltage in the ±3 V interval to screen the linear region of the films according to Ohm's law.

2.6.2 Cyclic Voltammetry

Two-electrode coin cells were fabricated with 3 mm discs of electrode material. Cyclic voltammetry (CV) and electrochemical impedance spectroscopy (EIS) measurements were carried out using a Biologic VMP-300 potentiostat. CV was carried out in a potential window of ±200 mV at scan rates ranging from 1 mV/s - 30000 mV/s. EIS was carried out in the frequency range 1 Hz – 7 MHz under a potential amplitude of 10 mV. Charge storage capacity and charge transfer resistance analysis was carried out using Biologic EC-Lab software.

2.7 Freeze-drying of macroporous microfiber composite scaffolds

A hyaluronic acid hydrogel was prepared using a modified carbodiimide chemistry process essentially as previously described[25,26]. Briefly, HA sodium salt (1.6–1.8 MDa, Streptococcus equi, 53747) was dissolved in dH20 at a concentration of 3 mg/ml. Adipic acid dihydrazide (ADH) was added as a crosslinker in excess (1.832 g ADH/ 0.5 g HyA) while 1-ethyl-3-(3-dimethylaminopropyl)

carbodiimide (EDAC) was used to activate the HA carboxylate groups (800 mg per 1 g HyA). The reaction was initiated by dropping the pH to 4 using 1 m HCL and crosslinking was carried out overnight. The next day the pH was adjusted to pH 7 and the HA solution was dialyzed in dialysis tubing (6–8 kDa MWCO) through 100 × 10−3 m NaCl for 24 h (x2), followed by 20% ETOH and finally dH20. At this point, collagen type-IV and fibronectin solutions were triturated at a concentration of 0.1 mg mL−1 within the HA solution. Subsequently, microfiber frameworks were placed within Teflon moulds, filled with the HA and HA Coll-IV/Fn solutions were freeze-dried (TF = -40 °C). The macroporous composite scaffold was formed via the freezing of HA, phase separation of the water into crystals, compaction of the HA polymer chains and evaporation of water crystals to create a porous structure. Scaffolds were subsequently rehydrated through 100% and 70% ETOH solutions overnight and immersed in an EDAC/N-hydroxysuccinimide solution to crosslink the ECM molecules within the freeze-dried scaffold. The scaffolds were washed with DPBS before being stored overnight at 4 °C prior to cellularization or characterization. Mechanical testing of the HA scaffolds was carried out in a Zwick mechanical testing unit in a uniaxial compression configuration in a PBS bath. Cylindrical HA samples were tested to 60% strain using a 5N load cell using a displacement rate of 100% strain/min and the Youngs Modulus calculated using the slope of the stress-strain curve between 1% and 10% strain.

2.9 Biocompatibility

Primary human spinal cord astrocytes (Isolated and cryopreserved by ScienceCell, USA) were grown in DMEM-Ham's F12 supplemented with 1% PS, FBS, and astrocyte growth supplement (ScienceCell, USA). Following plating, cells were cultured in growth media for 1 day before changing the media to a serum-free formula of DMEM-Ham's F12, 1% PS, L-Glutamine, N21 max (R&D Systems, UK), and 0.2% B27 supplement. To assess astrocyte compatibility, astrocytes (P3-6) were seeded at a density of approximately 10,000 cells per well in 96 well plates containing 6 mm PCL or MXene-PCL films. Immortalized microglial cells (IMGs) were used to model the compatibility of the MXene surfaces with microglia cells, due to the role the microglia have in activating inflammation responses in the brain. IMGs were seeded at a density of 100,000 cells per well in 96 well plates containing 6 mm PCL or PCL-MXene films. IMG growth medium consisted of DMEM-Ham's F12, 1% PS, 1% L-Glutamine and 5% FBS. SH-SY5Y neuronal cells (American type culture collection, USA) were used to model the compatibility of the MXene surfaces with neurons. 100,000 cells per well of P12-P16 neurons were seeded on 6 mm PCL or PCL-MXene films. Growth medium consisting of DMEM:Ham's F12 (50:50) containing 10% fetal bovine serum (FBS, Biosera, Ireland), 1% L-glutamine, and 1% penicillin-streptomycin (PS). In each case, cell-seeded films were cultured for 1 - 4 days in growth medium, with Alamar Blue assay-based analysis of metabolic activity at days 1 & 4 before being washed with PBS and fixed for immunohistochemical analysis using 4% PFA or frozen for DNA analysis.

2.10 Electrical Stimulation of MXene-microfiber/HA macroporous scaffolds

PCL-MXene scaffolds were manufactured with 500, 750 or 1000 µm fiber spacings. PCL controls were manufactured with 500 µm spacings, only. SH-SY5Y cells were seeded at a density of 500,000 cells per scaffold in 6 mm PCL or PCL-MXene scaffolds filled with the HA-ECM macroporous material. Following 24 hrs of culture in growth medium to enable cellular infiltration of the scaffolds, the cellularized scaffolds were transferred to 8 well plates and stimulated using protocols previously developed for the promotion of axonal growth[9]. Using an in-plate electrode system (8-well plate C-Dish, IonOptix), a 200 mV/mm pulsed electric signal was applied to the scaffolds using an external pacing controller (C-Pace EP, IonOptix), at a frequency of 12 Hz, a pulse duration of 50 ms on a continuous application for 6 days. Metabolic activity was measured at days 1, 3 and 7 and following

completion of the stimulation period, the scaffolds were washed with PBS and either fixed using 4% PFA for 1 hour for immunohistochemical analysis or frozen and stored for DNA quantification.

2.11 Assay analysis of cell growth

Metabolic Viability Assay Analysis: At selected time points an Alamar Blue assay (Invitrogen, UK) was performed according to the manufacturer's instructions. For each time point, films, coverslips or scaffold samples were washed with DPBS and immersed in a 10% Alamar Blue, 90% medium solution (500 µL per well, 1 h, 37 °C). The assay solution was pipetted in triplicate into an opaque 96-well plate and the absorbance of the solution was read at 563 nm to give a relative comparison of cellular metabolic activity of the cells. The coverslips/scaffolds were then washed in DPBS and re-immersed in the appropriate culture medium.

DNA Quantification: DNA quantification was performed using a Quant-IT Picogreen dsDNA assay kit (Invitrogen, UK) according to the manufacturer's instructions. Briefly, cells were lysed in 500 µL lysis buffer (0.2 m carbonate buffer containing 1% Triton-X100) and then underwent three freeze-thaw cycles at -80 °C to fully lyse all cells. Next, each sample was diluted 1:2 in 1× Tris-EDTA buffer before adding 100 µL of sample solution into an opaque 96-well plate in duplicate. Quant-iT dsDNA reagent was prepared by adding 100 µL to 19.9 mL of 1× Tris-EDTA buffer. Before adding 100 µL to each well-containing sample. The fluorescence of each sample was measured at an excitation wavelength of 485 nm and an emission wavelength of 538 nm. DNA concentration was calculated using a standard curve. Alamar blue and Picogreen results for each sample were used to calculate cell activity relative to cell DNA content.

2.12 Immunohistochemistry

Following fixation in 4% PFA (30 min, RT) and a DPBS wash step, astrocyte, microglia and neuron-seeded films, coverslips and scaffolds were permeabilized with 0.1% Triton X100– DPBS (30 min, RT), washed in DPBS before being incubated with blocking solution overnight at 4°C. Primary antibodies were then added as listed below and incubated overnight at 4°C. Samples were then washed in dPBS (x 3 times, 5 mins) before the addition of secondary antibody solution (listed below) and another overnight incubation step (4°C). Samples were washed and then incubated with Atto-Phalloidin (1:500, 2 h, RT) to highlight the actin skeleton before a further wash step and the incubation of samples with 4',6-diamidino-2-phenylindole (DAPI) (1:1000, up to 1 h, RT) to label the cell nuclei prior to 3 final wash steps. Coverslips and films were then mounted on glass slides for imaging using Fluoromount mounting medium (Invitrogen, UK).

Cell Type	**Primary Antibody**	**Concentration**	**Manufacturer**
Astrocytes	Mouse anti-GFAP	1:500	Sigma Aldrich, Ireland
IMG Microglia	Rabbit Anti-IBA-1	1:500	Abcam, UK
SH-SY5Y Neurons	Rabbit Anti-βIII tubulin	1:750	Sigma Aldrich, Ireland
Secondary Antibody			
Goat anti-rabbit 488		1:1000	Invitrogen, UK
Donkey anti-mouse 555		1:1000	Invitrogen, UK

Table 1. Immunohistochemistry primary and secondary antibodies.

Fluorescently labelled samples were imaged using a Zeiss 710 LSM NLO confocal microscope (Zeiss) at consistent exposure, gain, and magnification across all samples. The longest axon was measured

manually using FIJI tools in each field of view on the neuron-seeded scaffolds and calculated as an average per sample.

3.0 Results

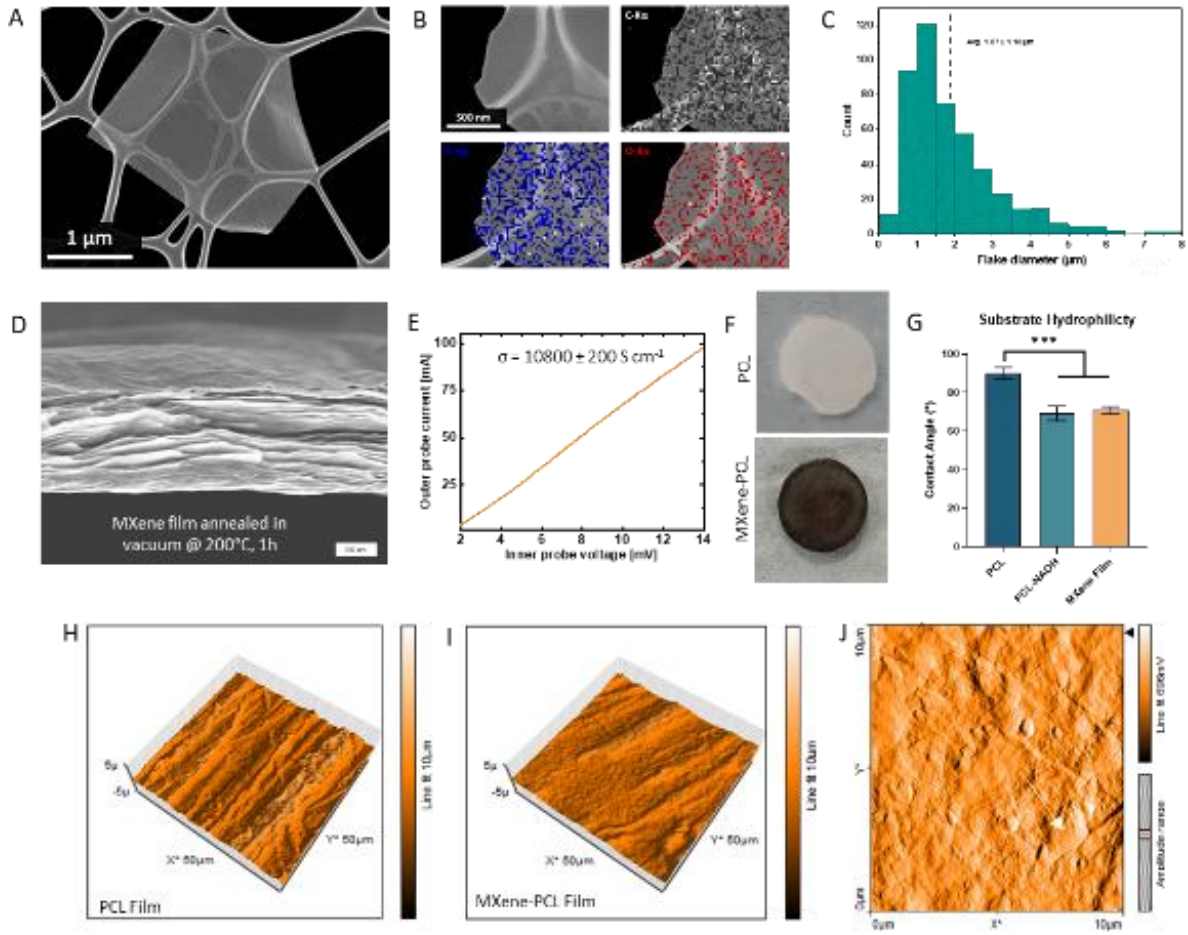

Figure 1. MXene material characterization. (A) SEM micrograph of MXene flake morphology and (B) EDX analysis of elemental composition. (C) Nanoparticle Size Distribution Measurements. (D) SEM of vacuum-annealed MXene film, demonstrating layered flake morphology. (E) Conductivity of annealed MXene films. (F) Coating of PCL films produces opaque black film. (G) NAOH-treated PCL surfaces exhibit similar hydrophilicity to MXene films.. Atomic Force Microscopy of tip-displacement analysis (H) PCL and (I) MXene-PCL films. (J) high-resolution deflection measurement of MXene-PCL surfaces.

3.1 MXene synthesis, characterization and PCL-MXene film formation

To produce conductive 2D MXene nanosheets, Al-rich Ti3AlC2 MAX phase powder was etched using 9M HCl and treated with LiF to produce etched multilayer $Ti_3C_2T_x$ MXene. The etched multilayer MXenes were then dispersed into delaminated sheets using vortex mixing and then concentrated using centrifugation to form a concentrated MXene ink. SEM analysis (Fig. 1(A)) of Al-rich Ti_3AlC_2 MXene flakes reveal the successful synthesis of 2D nanosheets with a micrometer scale diameter. EDX analysis (B) of the elemental composition of the flakes indicates the distribution of characteristic functional groups such as C-, Ti- and O-groups. The average flake diameter (C) was approximately 1.87 ± 1.18 µm. SEM analysis of annealed MXene films (D) demonstrates the nanoscale thinness of the sheets and the layered morphology of MXene films. Analysis of the conductivity (E) of the MXene

films indicated a high conductivity of approximately 10,800 ± 200 S/cm. To develop MXene-PCL composite materials (F) PCL films were dip-coated in the MXene inks to produce an opaque black MXene film. To improve the adhesion of the MXene nanosheets to the PCL surface, the PCL films were first treated with NAOH to improve the hydrophilicity of the film surface (G). AFM analysis of the NAOH-treated PCL films indicate a pitted polymer surface (H) while the MXene coating formed a scale-like coating along the fiber surface (I). In high-resolution phase-based imaging of the surface (J) the layered flake morphology of the MXene coatings can be clearly observed.

3.2 Neurocompatibility of MXene surfaces

To assess the biocompatibility of the MXene-PCL composites with key neural cell types, PCL and PCL-MXene films were seeded with neurons, microglia and astrocytes (Figure 2). All cell types exhibited widespread coverage of both the PCL and PCL-MXene films with confluent monolayers formed across both samples (Fig 2.(A - C)). Neurons exhibited neurite extension on both surfaces, indicative of biocompatibility on the surface. IBA-1 positive microglia proliferated across both materials. Astrocytes exhibited low levels of GFAP expression and extended processes across both PCL and MXene-PCL substrates, indicative of a non-cytotoxic cell-material interface. Measurement of neuronal metabolic activity (C) indicated an increased viability on MXene surfaces after 4 days of culture with a significant ($p<0.001$) 4.506 ± 1.02-fold change observed in the MXene-PCl samples at day 4 relative to PCL controls at Day 1, in comparison to a 2-fold change on PCL controls at day 4. Analysis of cell number (E) indicated that a large portion of this increase was due to increased neuronal proliferation with average DNA content increased on the MXene films from 282.45 ± 74.5 ng to 819.2± 168 ng per sample, an almost 10-fold increase in DNA, while PCL samples exhibited no increase in DNA content over time. Per-cell neuronal metabolic activity exhibited no significant change on PCL surfaces but significantly decreased in the PCL-MXene samples. Combined with the extensive coverage of the substrate with neurons with healthy morphologies these results suggest that the MXene surfaces promoted the rapid formation of a confluent neuronal monolayer and that cell-cell contacts and possibly neuronal differentiation due to the conductive nature of the film lead to increases in DNA content, but decreases in per-cell metabolic activity.

Microglial cells exhibited no significant changes in metabolic activity between groups, although a trend towards increased metabolic activity on PCL-MXene samples was observed and microglia proliferated evenly over both samples. These data indicate the MXenes exhibit low cytotoxicity but the rounded morphology of microglia in both samples is indicative of an activated state – but further analysis is necessary to ascertain whether this is indicative of an M1 pro-inflammatory or M2 pro-reparative phenotype[27]. Astrocyte viability was significantly increased at day 4 ($p<0.001$), reflective of significantly higher astrocyte coverage of the PCL-MXene films.

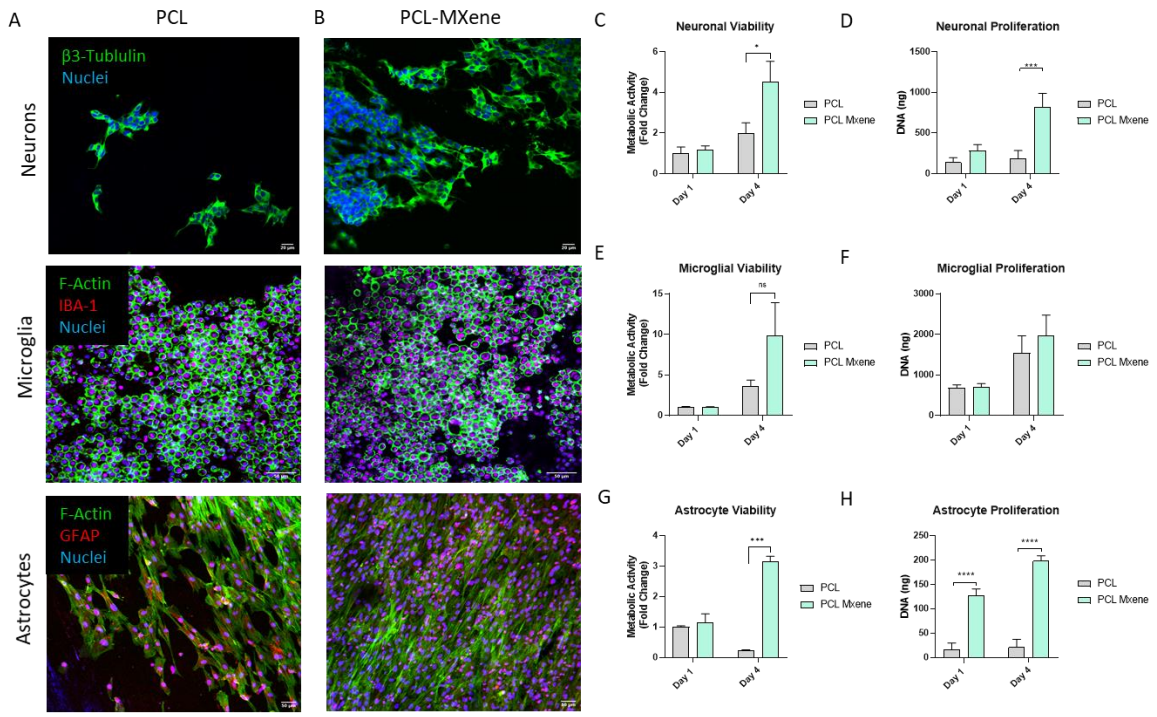

Figure 2. MXene-PCL Biocompatibility. (A) Immunolabelling of cell morphologies reveals excellent compatibility of SH-SY5Y neurons, microgia and astrocytes with (A) PCL films and (B) MXene-PCL films. Neurons exhibit increased coverage of the MXene films and project neurites along both the MXene-PCL and PCL surfaces – indicative of biocompatibility. IBA-1-positive Microglia formed multi-layered confluent aggregates covering both PCL and MXene-PCL surfaces, indicative of low cytotoxicity. Astrocytes exhibited improved coverage of the PCL-MXene surfaces, indicative of improved biocompatibility compared to PCL controls. Neurons exhibited enhanced viability (C) and proliferation (D) on MXene-PCL surfaces compared to PCL controls. Similarly microglia exhibited increased viability(E) on MXene-PCL surfaces although no difference in proliferation (F) was observed. Astrocytes exhibited increased metabolic activity after 4 days on the MXene-PCL surfaces and significantly higher cell attachment, driving an increase in cell number by day 4. Scale bars = 50 µm

3.3 Manufacture and characterization of MXene functionalized MEW architectures.

Shaper software (RegenHu, Switzerland) (Figure 3 (A)) was used to design microfiber architectures containing rectilinear box-like architectures with 1000, 750 and 500 µm fiber spacings to produce MEW scaffold architectures with varying fiber densities (B) resulting in significant changes in the effective cross-sectional areas of the scaffolds across each horizontal axis (C). The direction of the infill was rotated by 90° for every second layer (D) and the MEW parameters (E) were optimized to produce high fiber resolution and an average fiber diameter (n=8) of approximately 13.64 ± 0.64 µm. 6 mm scaffolds were punched from 20 mm x 20 mm x 750 µm meshes and exhibited a high degree of spatial resolution across each fiber architecture (F). Dip coating of NAOH-treated scaffolds in 1 mg/ml MXene suspensions formed a black MXene film along the fiber surface. SEM analysis of the PCL and MXene-PCL fiber architectures (G) indicated that MXene coatings were spread evenly across the PCL fibers at each fiber density with the 2D flakes forming a thin scale-like crust across the fiber surface (H, I). MXene nanosheets exhibited flat, flake-like morphologies, adhering in dense overlapping layers close to the fiber surface and examination of the cross-sections of MXene-coated fibers demonstrate that the MXene treatment produced films consisting of multiple overlapping layers of MXene sheets. This layered film increased in consistency and thickness over each dip-coating resulting in significant increases in bulk conductivity (J) with each coating ($p<0.05$). The conductivity of the less dense 1000 µm spacing architectures increased from approximately

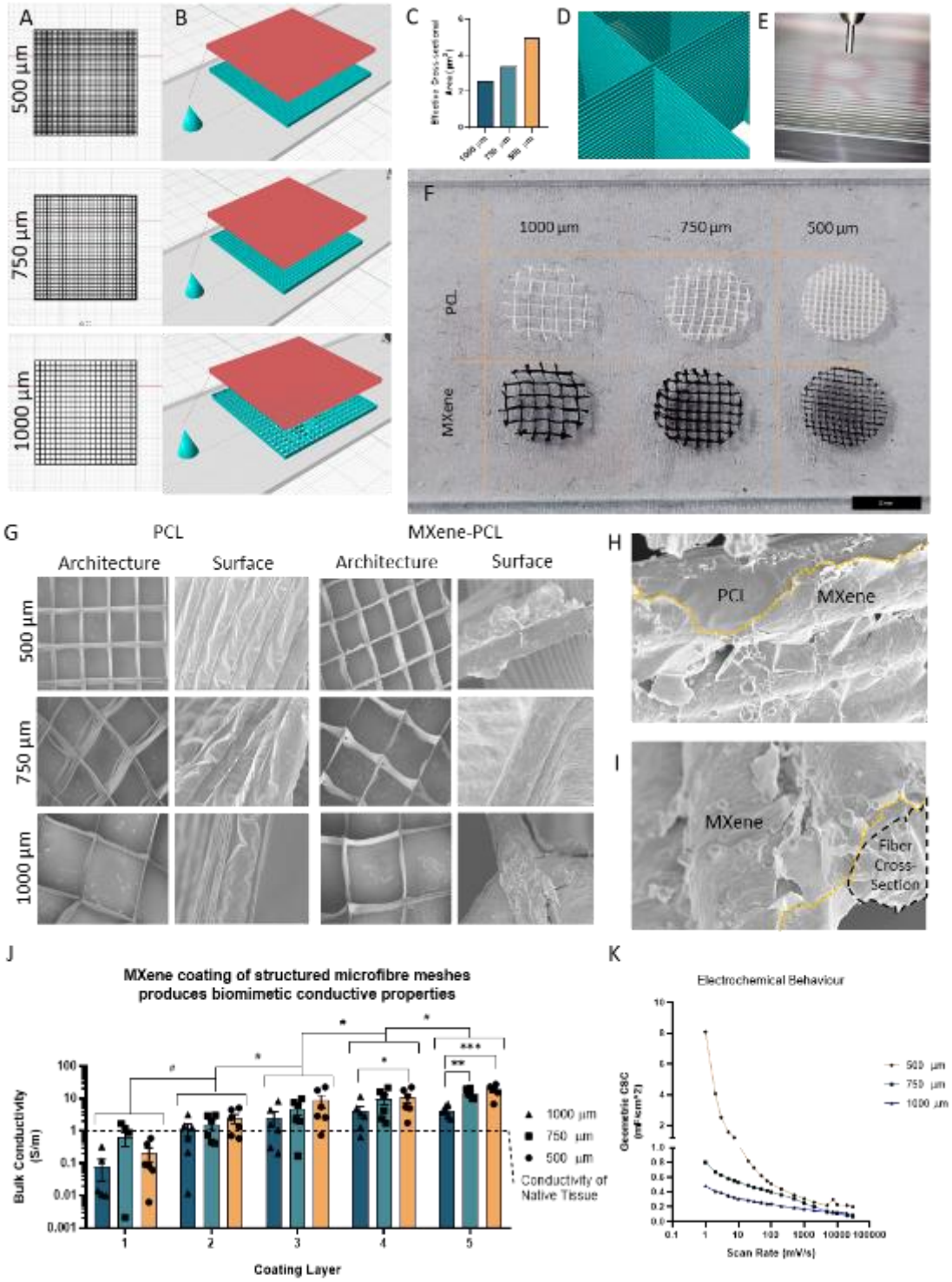

Figure 3. Melt Electrowriting of PCL-MXene microfibre meshes. (A) Design of microfibre meshes of varying pore size. (B) SHAPR modelling of spinneret movement (red) and projected mesh design (teal). (C) Variation in fiber spacing results in significant changes in cross-sectional area. (D) Meshes are formed from interwoven laters of microfibers to a height of 75 layers. (E) Optimization of fiber deposition parameters results in high resolution printing. (F) Photos of 500, 750 and 1000 um meshes. (G) Corresponding SEM micrographs of PCL and PCL-MXene microfiber architecures, demonstrating effective production of 500, 750 and 1000 um mesh-spacings. (H) MXene coatings result in homogenous adherence of MXene flakes to the PCL surface, which form (I) a thin intercalated crust. (J) The conductivity of PCL-MXene meshes is dependent on microfiber density ($p<0.001$) and MXene layer thickness ($p<0.001$). (KJ) Analysis of the electrochemical behaviour of MXene microfiber architectures using cyclic voltammetry.

0.081 ± 0.053 S/m to 4.252 ± 0.67 S/m, while the 750 µm scaffolds increased from 0.63 ± 0.3 S/m to 14.63 ± 1.93 S/m and the dense 500 µm scaffolds increased from 0.2 ± 0.1 to 18.87 ± 2.94 S/m resulting in the highest bulk conductivity over all. 2-way ANOVA analysis indicated that both fiber density and coating layers significantly influenced the bulk conductivity of the scaffolds indicating that the electrical properties of the resulting architectures dependent both on MXene treatment and scaffold architecture, with conductivity roughly proportional to the cross-sectional area of fibers in the direction of measurement. Finally, the electrochemical properties of the scaffolds were analysed through cyclic voltammetry (K) and measurement of the specific capacitance indicated that, despite the low density of the conductive microfibers, the specific capacitance of the microfiber architectures (0.3 – 1.05 mF/cm², 1000 – 500 µm), exhibited similar capacitance to commercial platinum electrodes (approx. 0.1 – 0.2 mF/cm²) at 10 mV/s scan rates[28,29] and gold electrode arrays (0.11 mF/cm²), although was significantly lower than nanofibrous conductive textiles (e.g. PEDOT carbon fabric 70 mF/cm²)[29] and CNT-based microelectrode arrays (1.51 mF/cm²)[30].

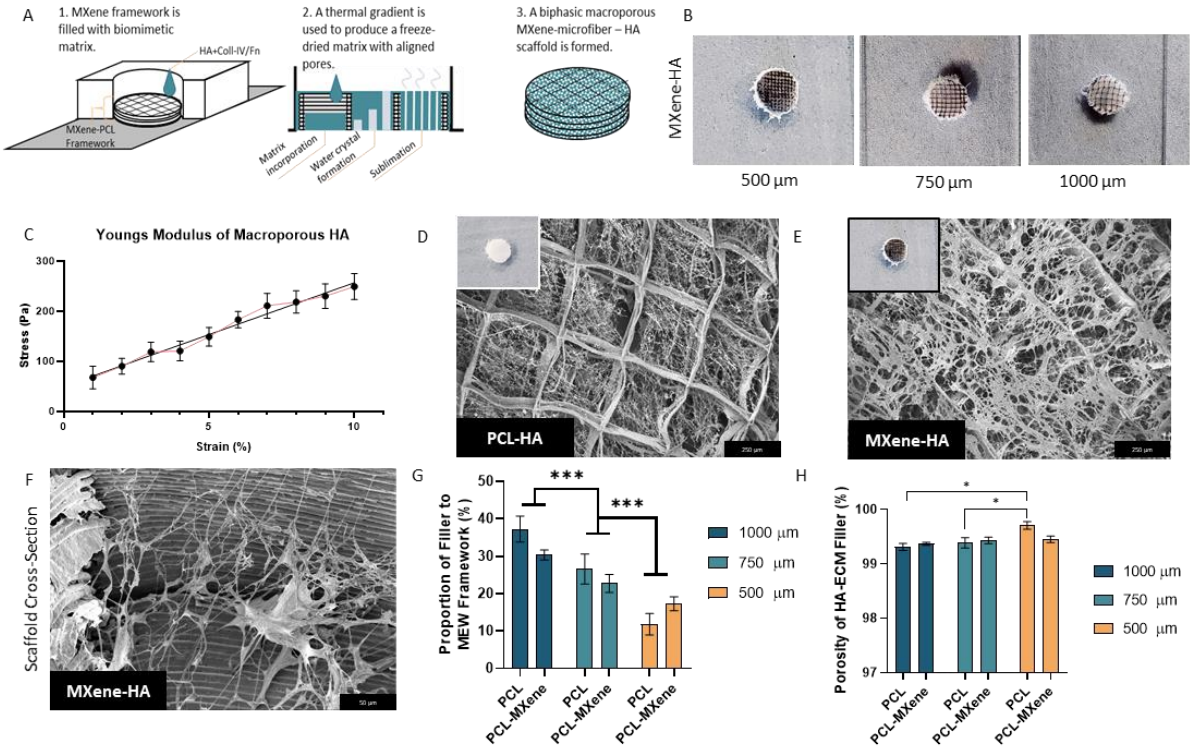

Figure 4. Freeze drying and characterization of HA-ECM filler material within MEW frameworks. (A) Schematic diagram detailing manufacturing process. (B) Photos of 500, 750 and 1000 µm HA-filled frameworks. (C) Uniaxial compression testing of 3 mg/ml HA scaffolds. (D-F) SEM micrograph of biphasic scaffolds. (D) PCL-HA (E) MXene-HA scaffold. (F)MXene-HA scaffold cross-section. (G) Proportion of HA filler decreases with increasing fiber density. (H) All scaffolds exhibited high (>99%) porosity with small but significant trends towards increased porosity in denser fiber architectures.

3.4 Manufacture and Characterization of MXene-microfiber-reinforced Hyaluronic Acid Scaffolds.

A hydrazide-modified HA hydrogel was synthesized and triturated with 100 µg/ml each of Collagen Type-IV and Fibronectin[26] (Figure 4 (A)), proteins native to the central nervous system which we have previously demonstrated exhibit synergistic neurotrophic signalling. PCL and MXene-PCL microfiber architectures were then placed in 6 mm Teflon moulds with stainless steel bases and the

microfiber architecture filled with the HA-ECM material. The moulds were flash-frozen to induce orientated water crystal growth and then freeze-dried to form a macroporous HA-ECM phase within the microfiber frameworks (B). The macroporous HA-ECM material exhibited a biomimetic Young's Modulus of approximately 1.51 ± 0.3 kPA, matching the approximate softness of native brain tissue[31,32] and within a similar range to what we've previously shown promotes axonal growth[25]. SEM analysis of PCL-HA (D) and MXene-PCL-HA (E) samples demonstrated the incorporation of the macroporous HA-ECM material throughout the microfiber architectures. Examination of the scaffold cross-section was indicative of an orientated pore architecture in the voids between the fibers. The scaffolds exhibited decreasing proportions of the HA filler with increasing fiber density but the average porosity of the macroporous material was above 99% in each sample, indicative of a highly porous environment. Porosity was significantly higher in the 500 µm architectures ($p<0.05$).

3.5 Electrical stimulation of cellularised MXene-microfiber-reinforced Hyaluronic Acid Scaffolds.

SH-SY5Y neurons were seeded in PCL-500 µm and MXene-500 µm scaffolds (n=12 per group) and cultured in differentiation medium for 7 days or stimulated in an IonOptix bioreactor (Figure 5 (A)). Stimulated scaffolds exhibited robust cellular growth in all groups (B) with excellent coverage of each scaffold and longer, denser neurites visible in both stimulated and non-stimulated MXene-functionalized samples. Metabolic activity increased in all groups throughout the experiment and was highest in the MXene-functionalized, non-stimulated samples. No significant change in cell number was observed between all groups, but the per-cell metabolic activity was significantly lower ($p<0.01$) in stimulated MXene-functionalized scaffolds compares to stimulated PCL samples. Analysis of the formation and maximal extension of the longest axon in each sample indicated that the longest axons were observed in the electrically stimulated MXene-functionalized samples (108.5 ±6.13 µm), in which axons were significantly ($p<0.01$) longer, on average, compared to PCL controls (74.3 ±5.78 µm) and non-stimulated MXene samples (67.41 ±6.52µm). These results indicate that the presence of a MXene-functionalized microfiber network enhance the provision of electrical stimulation to neurons compared to inert PCL microfibers.

3.6 The influence of MXene microfiber architecture on ES delivery to neurons

Extensive interconnected neurite networks were observed in all samples wherever dense cell numbers were observed. No significant difference between metabolic activity was observed between different fiber architectures over time, although metabolic activity increased throughout the stimulation period. The DNA content of samples was proportional to the fiber density with 500 µm samples exhibited significantly higher DNA content compared to 1000 µm samples. The longest axons were observed in the 750 µm architectures and were significantly longer (134.9 ±16.81, $p<0.05$) than those observed in the 1000 µm architecture (95.94 ±7 µm) with no significant increase over 500 µm samples.

4.0 Discussion

The main objective of this study was to investigate whether microscale distribution of conductive biomaterials can be used to enhance the axonal growth-promoting effects of electrical stimulation of neurons. These data demonstrate that the high spatial resolution of melt electrowriting combined with adhesive nature of MXene nanosheets can be used to produce tunable conductive MXene-PCL microfiber architectures, with fiber spacing used to control electrical properties such as bulk conductivity and geometric charge storage capacity. MXene surfaces exhibited excellent compatibility with neurons, astrocytes and microglia. The incorporation of a biomimetic ECM within the microfiber architecture allowed the indirect stimulation of cells in an environment similar to native tissue.

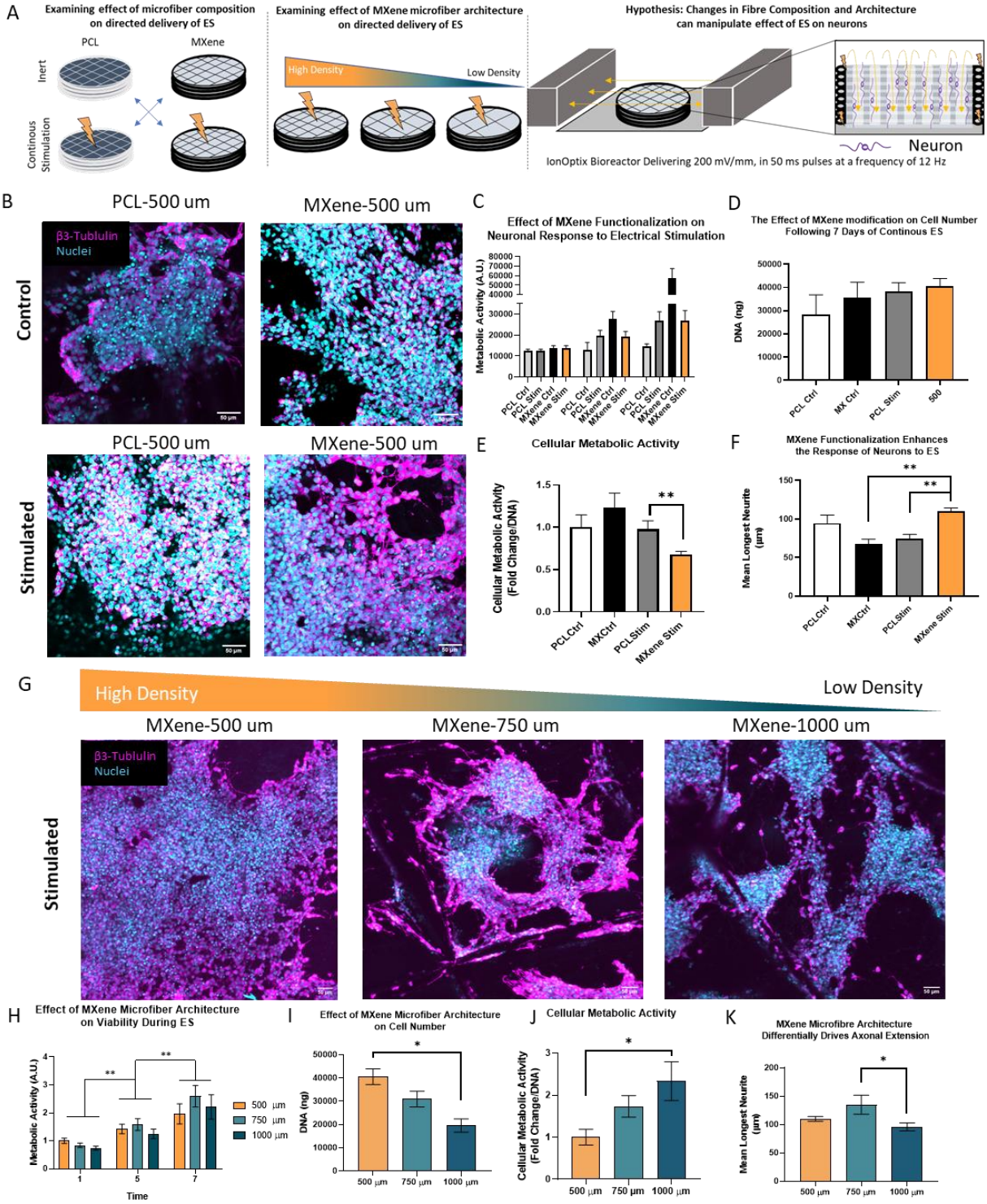

Figure 5. The Effect of Microfiber Scaffold Conductivity and Architecture on Neuronal Cell Behaviour in Response to Continuous Electrical stimulation. (A) Schematic Diagram of Experimental Approach (B) Immunohistochemical analysis of neuronal cell morphology (DAPI/BIII Tubulin). (C) Analysis of metabolic activity indicated excellent tolerance of the simulation and increased metabolic activity on MXene microfiber-reinforced scaffolds compared to PCL controls. Overall, cellular metabolic activity was significantly decreased on stimulated MXene scaffolds compared to stimulated PCL scaffolds indicative of significant impact of the conductivity of the scaffold on the delivery of ES to neurons. (F) Stimulated MXene scaffolds exhibited longer neurites than stimulated PCL scaffolds or MXene controls. (G) MXene microfiber density exerted significant effects on cell morphology with more neurites visible in higher density (500 um, 750 um) scaffolds compared to low density scaffolds (1000 um). No significant effects on total metabolic activity were observed over 7 days, although the increase in metabolic activity over time indicated that the ES regime was not cytotoxic. There were larger numbers of cells present on the higher density frameworks after 7 days, but these cells exhibited significantly lower levels of metabolic activity. (K) The longest axons were observed in 750 um density scaffolds which exhibited significantly longer axons compared to the 1000 um group.

Continuous electrical stimulation of neurons within the conductive architectures significantly increased axonal growth compared to stimulated neurons in scaffolds containing inert PCL fibers. Furthermore, viability and axonal growth response of neurons to ES delivery was dependent on the conductive microfiber architecture. Taken together, these results indicate that combining MEW microfiber printing and MXene nanosheet functionalization results in highly tunable biphasic conductive scaffolds which can be used to control and direct the delivery of ES to neurons within a tissue engineering scaffold and offers a novel biofabrication-enables approach for the targeted delivery of growth-promoting electrical stimulation to neurons.

This study utilizes $Ti_3C_2T_x$ MXene nanoflakes as a novel method for the functionalization of MEW microfiber scaffolds enabling the production of highly conductive ordered structures with microscale distribution of conductive materials. The use of a microfibrous PCL-MXene composite results in a highly contiguous network of intercalated MXene flakes and enables the manufacture of scaffolds whose bulk conductivity is far higher (approx. 19 S/m) than native tissue (approx. 0.4 S/m[33]) but which requires a relatively low mass of conductive nanomaterials to achieve this conductivity. Furthermore, the tunable electrochemical properties of the MXene architectures alongside their relatively high geometric capacitance indicate potential for the use of high density MXene-microfiber biomaterials in neural electrode applications e.g. electrocorticography recording devices[28,32,34].

By confining the MXene nanosheets within the scaffold to dense coatings of the slow-degrading PCL microfiber architectures[35], the volume ratio of MXenes required to produce a conductive network throughout a scaffold is efficiently minimized, while the highly porous nature of the microfiber scaffolds allows the incorporation of a biomimetic filler material to enhance regeneration and enables the growth of tissue and cells through the scaffold in response to electrical stimulation, while preserving conductive material characteristics. The results show that the neurons exhibit robust growth throughout the biomimetic phase of the scaffold while also benefitting from the capacity of the conductive microarchitecture to enhance the delivery of ES throughout the implant. In contrast, existing conductive scaffold designs (such as PEDOT hydrogels[21]) provide a poor template for regeneration due to a lack of natural ligands and poor degradation properties. Furthermore, conductive polymers exhibit poor processability, and are incompatible with traditional electrohydrodynamic processing due to arcing, are challenging to 3D print and often require cytotoxic crosslinkage (e.g. heat-activated chemical crosslinkage[20].

The high conductivity of MXene nanosheets combined with their stability and biocompatibility makes them an attractive conductive biomaterial[11,36]. This study demonstrates that MXenes provide an excellent substrate for promoting neuronal, astrocyte and microglial growth, with each cell type exhibiting high metabolic activity compared to PCL controls. Previous work on the use of MXene films for enhancing electrical stimulation has demonstrated their capacity to effectively enhance the stimulation of iPSC-derived cardiomyocytes[24] and neural progenitor cells[11]. These findings align with the broader literature on the use of MXenes in biological applications. Zhu et al. (2023) recently coated electrospun PLLA microfibers with MXenes and demonstrated that their innate material characteristics (e.g. conductivity) could promote neuronal differentiation of neural progenitor cells and that MXenes did not provoke a strong foreign body response following subcutaneous implantation. While the use of MXenes in melt electrowritten scaffolds has seen limited implementation to-date[37], Li et al. (2024) coated PCL microfibers with MXenes and demonstrated that the MXene-microfibers could be used to deliver optocapacitance-based neuronal stimulation[38]. Conductive MEW scaffolds for tissue engineering applications have previously been developed utilizing conductive polymer (e.g. polypyrrole)[39] and metallic (e.g. gold)[40] coatings. However, conductive polymers such as polypyrrole exhibit rapid degradation due to oxidation and leaching of

dopants, making them unsuitable for long-term use in an in vivo environment, while the aluminium-rich MAX-phase-derived $Ti_3C_2T_x$ MXenes utilized in this study exhibit excellent long-term stability in aqueous environments[36].

The biomimetic HA Coll-IV/Fn macroporous filler material used in this study exhibits a similar softness to the native brain tissue and the functionalization of HA with collagen type-IV and fibronectin synergistically enhances axonal growth – making it an excellent substrate for trialling therapeutic electrical stimulation strategies[25]. The optimized and defined ECM content of the scaffold is a significant advance over previously developed scaffolds for in vitro 3D cell culture which utilized Matrigel or thiolated HA[41–43]. While these studies indicate that microfiber reinforcement of soft materials can enhance their capacity to facilitate neural tissue development, Matrigel is unsuitable for clinical application due to its highly variable composition and HA-alone exhibits limited bioactivity mainly through CD44 binding, which is further limited by the use of bioactive functional groups (e.g. hydroxyl groups) in cross-linking to form hydrogels[44]. In contrast the biphasic scaffold presented in this study possesses a composition optimized for promoting pro-reparative behaviour in neural applications and exhibits a macroporous architecture that can provide physical cues to drive axonal growth through the pore architecture – enhancing its capacity to act as a pro-regenerative implant for neurotrauma repair.

In the microfiber-reinforced scaffold system described in this study, the majority of neurons are not in direct contact with the conductive material phase but the results show that MXene microfiber architectures broadly influence ES delivery to neurons. Previous work by Zhang et al.(2018) has shown that patterning of 3D electrodes in 3D biomaterial environments can manipulate electrical fields to influence axonal growth and cell aggregation[6]. As such, the density of fibers throughout the scaffold influences not only the conductance of charge across the scaffolds but can also manipulate electric fields throughout the conductive architecture. While modelling how the changes in conductive architecture influence electric charge distribution and electric field formation throughout the scaffold is beyond the scope of the current study, our data demonstrates that the distribution of conductive materials throughout the scaffold has significant influence on cell morphology, neuronal growth and axonal growth and that, of the three fiber designs tested, the 750 µm architectures provided optimal axonal growth. The measured difference in bulk conductivity between the 750 µm scaffolds and 500 µm scaffolds were not significant and the increased proportion of neurotrophic material in the 750 µm scaffolds may be indicative of a trade-off between the benefits of the conductive phase and the provision of the orientated HA-ECM environment to harness and guide the growth-promoting effects of ES.

This study demonstrates the design, manufacture, characterization and in vitro testing of the capacity of a novel conductive 3D printed scaffold to promote axonal growth. However, one of the key benefits of electrical stimulation is its potential to promote multiple aspects of repair beyond axonal growth including neural plasticity and promoting stem cell differentiation. Furthermore, this study investigates one stimulation regime applied to cells within the conductive scaffolds. While the synergistic interactions between conductive microarchitectures and ES observed in this study have important implications for conductive implant design, it is likely that the stimulation profile could be optimized for other aspects of regeneration as the response of cells to electrical stimulation regimes is highly variable[45]. Future work will examine the response of primary neuronal and stem cell cultures in MXene microfiber composite scaffolds with the aim of developing multifunctional electroactive implants to drive neurotrauma repair.

5. Conclusion

This study describes the development of melt electrowritten MXene-PCL microfiber architectures with tunable electrical properties. These conductive architectures were incorporated within a biomimetic macroporous biomaterial to form composite scaffolds which enhanced the delivery of electrical stimulation to neurons, resulting in improved axonal growth. The delivery of ES was dependent on the microfiber architecture of the scaffolds, providing a template for the design of more effective use of electroactive biomaterials in neural regeneration. This novel system combines cutting-edge 2D nanomaterials with microscale biofabrication and biomimetic macroporous HA biomaterials to produce a multifunctional conductive scaffold with significant implications for the future development of electrically active neural implants for the repair of lesions associated with neurotrauma.

Acknowledgements:

This study was funded by a joint funding initiative of the Irish Rugby Football Union Charitable Trust (IRFU-CT) and the Advanced Materials and Bioengineering Research (AMBER) Centre through Science Foundation Ireland (SFI/12/RC/2278) as well as by an Irish Research Council Postdoctoral Fellowship (Government of Ireland), Grant Number: GOIPD/2021/262, an EPSRC/SFI Centre for Doctoral Training in the Advanced Characterisation of Materials: 18/EPSRC-CDT/3581 15735. The authors thank the Advanced Microscopy Lab (AML) at the Centre for Research on Adaptive Nanostructures and Nanodevices (CRANN) for their help with the performance of electron microscopy.

References:

1. Rubiano, A. M., Carney, N., Chesnut, R. & Puyana, J. C. Global neurotrauma research challenges and opportunities. *Nature* **527**, S193–S197 (2015).

2. Matney, C., Bowman, K. & Berwick, D. Traumatic brain injury: A roadmap for accelerating progress. (2022).

3. Griffin, J. M. & Bradke, F. Therapeutic repair for spinal cord injury: combinatory approaches to address a multifaceted problem. *EMBO Mol Med* **12**, e11505 (2020).

4. McGuire, T. K., Stasiewicz, M., Woods, I., Dervan, A. G. & O'Brien, F. J. Biomaterial-Based Gene Delivery to Central Nervous System Cells for the Treatment of Spinal Cord Injury. *Advanced NanoBiomed Research* **n/a**, 2300030.

5. Siddiqui, A. M. *et al.* Newly regenerated axons via scaffolds promote sub-lesional reorganization and motor recovery with epidural electrical stimulation. *npj Regen Med* **6**, 1–12 (2021).

6. Zhang, Q. *et al.* Electrical Stimulation with a Conductive Polymer Promotes Neurite Outgrowth and Synaptogenesis in Primary Cortical Neurons in 3D. *Sci Rep* **8**, 9855 (2018).

7. Marquez-Chin, C. & Popovic, M. R. Functional electrical stimulation therapy for restoration of motor function after spinal cord injury and stroke: a review. *BioMedical Engineering OnLine* **19**, 34 (2020).

8. Lorach, H. *et al.* Walking naturally after spinal cord injury using a brain–spine interface. *Nature* **618**, 126–133 (2023).

9. Maughan, J. *et al.* Collagen/pristine graphene as an electroconductive interface material for neuronal medical device applications. *Applied Materials Today* **29**, 101629 (2022).

10. Zhao, Y. *et al.* Application of conductive PPy/SF composite scaffold and electrical stimulation for neural tissue engineering. *Biomaterials* **255**, 120164 (2020).

11. Guo, R. *et al.* 2D Ti3C2TxMXene couples electrical stimulation to promote proliferation and neural differentiation of neural stem cells. *Acta Biomaterialia* **139**, 105–117 (2022).

12. Zhu, R. *et al.* Electrical stimulation affects neural stem cell fate and function in vitro. *Experimental Neurology* **319**, 112963 (2019).

13. Zhang, J. *et al.* Conductive Composite Fiber with Optimized Alignment Guides Neural Regeneration under Electrical Stimulation. *Adv Healthc Mater* **10**, e2000604 (2021).

14. Song, S. *et al.* Electrical stimulation of human neural stem cells via conductive polymer nerve guides enhances peripheral nerve recovery. *Biomaterials* **275**, 120982 (2021).

15. Xu, J., Wong, C.-W. & Hsu, S. An Injectable, Electroconductive Hydrogel/Scaffold for Neural Repair and Motion Sensing. *Chem. Mater.* **32**, 10407–10422 (2020).

16. Yan, L. *et al.* Adhesive and conductive hydrogel-based therapy simultaneously targeting neuroinflammation and neurofunctional damage after brain injury. *Nano Today* **51**, 101934 (2023).

17. Krauss, J. K. *et al.* Technology of deep brain stimulation: current status and future directions. *Nat Rev Neurol* **17**, 75–87 (2021).

18. Xie, Y. *et al.* In vivo monitoring of glial scar proliferation on chronically implanted neural electrodes by fiber optical coherence tomography. *Frontiers in Neuroengineering* **7**, (2014).

19. Kaur, G., Adhikari, R., Cass, P., Bown, M. & Gunatillake, P. Electrically conductive polymers and composites for biomedical applications. *RSC Adv.* **5**, 37553–37567 (2015).

20. Guex, A. G. *et al.* Highly porous scaffolds of PEDOT:PSS for bone tissue engineering. *Acta Biomater* **62**, 91–101 (2017).

21. Serafin, A. *et al.* Electroconductive PEDOT nanoparticle integrated scaffolds for spinal cord tissue repair. *Biomater Res* **26**, 63 (2022).

22. Ryan, A. J. *et al.* Electroconductive Biohybrid Collagen/Pristine Graphene Composite Biomaterials with Enhanced Biological Activity. *Advanced Materials* **30**, 1706442 (2018).

23. Lee, C.-Y., Sayyar, S., J. Molino, P. & G. Wallace, G. A robust 3D printed multilayer conductive graphene/polycaprolactone composite electrode. *Materials Chemistry Frontiers* **4**, 1664–1670 (2020).

24. Asaro, G. A. *et al.* MXene functionalized collagen biomaterials for cardiac tissue engineering driving iPSC-derived cardiomyocyte maturation. *npj 2D Mater Appl* **7**, 1–13 (2023).

25. Woods, I. *et al.* Biomimetic Scaffolds for Spinal Cord Applications Exhibit Stiffness-Dependent Immunomodulatory and Neurotrophic Characteristics. *Advanced Healthcare Materials* **11**, 2101663 (2022).

26. O'Connor, C., Woods, I., Hibbitts, A., Dervan, A. & O'Brien, F. J. The Manufacture and Characterization of Biomimetic, Biomaterial-Based Scaffolds for Studying Physicochemical Interactions of Neural Cells in 3D Environments. *Current Protocols* **3**, e688 (2023).

27. Lauro, C. & Limatola, C. Metabolic Reprograming of Microglia in the Regulation of the Innate Inflammatory Response. *Front. Immunol.* **11**, (2020).

28. Oribe, S. *et al.* Hydrogel-Based Organic Subdural Electrode with High Conformability to Brain Surface. *Sci Rep* **9**, 13379 (2019).

29. Terutsuki, D. *et al.* Totally Organic Hydrogel-Based Self-Closing Cuff Electrode for Vagus Nerve Stimulation. *Advanced Healthcare Materials* **11**, 2201627 (2022).

30. Yang, H. *et al.* Carbon Nanotube Array-Based Flexible Multifunctional Electrodes to Record Electrophysiology and Ions on the Cerebral Cortex in Real Time. *Advanced Functional Materials* **32**, 2204794 (2022).

31. Saxena, T., Gilbert, J., Stelzner, D. & Hasenwinkel, J. Mechanical characterization of the injured spinal cord after lateral spinal hemisection injury in the rat. *J Neurotrauma* **29**, 1747–1757 (2012).

32. Go, G.-T., Lee, Y., Seo, D.-G. & Lee, T.-W. Organic Neuroelectronics: From Neural Interfaces to Neuroprosthetics. *Advanced Materials* **34**, 2201864 (2022).

33. McCann, H., Pisano, G. & Beltrachini, L. Variation in Reported Human Head Tissue Electrical Conductivity Values. *Brain Topogr* **32**, 825–858 (2019).

34. Wang, K. *et al.* High-Performance Graphene-Fiber-Based Neural Recording Microelectrodes. *Advanced Materials* **31**, 1805867 (2019).

35. Dias, J. R., Sousa, A., Augusto, A., Bártolo, P. J. & Granja, P. L. Electrospun Polycaprolactone (PCL) Degradation: An In Vitro and In Vivo Study. *Polymers* **14**, 3397 (2022).

36. Mathis, T. S. *et al.* Modified MAX Phase Synthesis for Environmentally Stable and Highly Conductive Ti3C2 MXene. *ACS Nano* **15**, 6420–6429 (2021).

37. Saiz, P. G., Reizabal, A., Vilas-Vilela, J. L., Dalton, P. D. & Lanceros-Mendez, S. Materials and Strategies to Enhance Melt Electrowriting Potential. *Advanced Materials* **n/a**, 2312084.

38. Li, J. *et al.* 3D Printed Ti3C2Tx MXene/PCL Scaffolds for Guided Neuronal Growth and Photothermal Stimulation. 2023.08.28.555002 Preprint at https://doi.org/10.1101/2023.08.28.555002 (2023).

39. Olvera, D., Molina, M. S., Hendy, G. & Monaghan, M. G. Electroconductive Melt Electrowritten Patches Matching the Mechanical Anisotropy of Human Myocardium. *Advanced Functional Materials* **30**, 1909880 (2020).

40. Zhang, Y., Le Friec, A., Sun, D. & Chen, M. Sinusoidal stretchable fibrous electrodes regulate cardiac contraction. *Chemical Engineering Journal* **455**, 140555 (2023).

41. Fischhaber, N. *et al.* Spinal Cord Neuronal Network Formation in a 3D Printed Reinforced Matrix—A Model System to Study Disease Mechanisms. *Advanced Healthcare Materials* **10**, 2100830 (2021).

42. Janzen, D. *et al.* Cortical Neurons form a Functional Neuronal Network in a 3D Printed Reinforced Matrix. *Advanced Healthcare Materials* **9**, 1901630 (2020).

43. Janzen, D. *et al.* Reinforced Hyaluronic Acid-Based Matrices Promote 3D Neuronal Network Formation. *Advanced Healthcare Materials* **11**, 2201826 (2022).

44. Kwon, M. Y. *et al.* Influence of hyaluronic acid modification on CD44 binding towards the design of hydrogel biomaterials. *Biomaterials* **222**, 119451 (2019).

45. Bertucci, C., Koppes, R., Dumont, C. & Koppes, A. Neural responses to electrical stimulation in 2D and 3D in vitro environments. *Brain Research Bulletin* **152**, 265–284 (2019).